INTERNATIONAL JOURNAL OF
COASTAL, OFFSHORE & ENVIRONMENTAL ENGINEERING IJCOE Vol.11 /No.1 /Winter 2026 (57-69)

Available online at: www. ijcoe.org

Deterministic Tsunami Hazard Assessment for a Nearshore–Onshore Domain close to the Strait of Hormuz: The Overlooked Threat of the Western Makran Segment and Tidal Sensitivity

Mohammad Hossein Kazeminezhad [1*]; Mahmood Reza Akbarpour Jannat [2]; Ehsan Rastgoftar[3]

[1*]*Iranian National Institute for Oceanography and Atmospheric Science, No.3, Etemad Zadeh St., Fatemi Ave, P.C: 1411813389, Tehran, Iran, E-mail: mkazeminezhad@inio.ac.ir*
[2]*Iranian National Institute for Oceanography and Atmospheric Science, No.3, Etemad Zadeh St., Fatemi Ave, P.C: 1411813389, Tehran, Iran, E-mail: akbarpour@inio.ac.ir*
[3]*Iranian National Institute for Oceanography and Atmospheric Science, No.3, Etemad Zadeh St., Fatemi Ave, P.C: 1411813389, Tehran, Iran, E-mail: e.rastgoftar@inio.ac.ir*

ARTICLE INFO

Article History:
Received:31 Aug 2025
Accepted:14 Jan 2026

Keywords:
Makran Subduction Zone
Tsunami Modeling
Strait of Hormuz
Tidal Sensitivity
Hydrodynamic Loads

ABSTRACT

The Makran Subduction Zone (MSZ) represents a critical tsunamigenic structure in the northwestern Indian Ocean. While the historical seismicity of the eastern segment has been extensively studied following the 1945 earthquake, the hazard potential of the western segment, specifically its threat to strategic energy infrastructure near the Strait of Hormuz, remains poorly constrained. This study presents a high-resolution deterministic tsunami hazard assessment for the Kooh Mobarak coastal onshore developments and its associated marine facilities. Utilizing the ComMIT/MOST numerical model within a nested grid framework, twelve fault rupture scenarios ranging from M_w 8.0 to 9.0 were simulated across the western, central, and eastern Makran segments. The results challenge conventional hazard zonations, demonstrating that a rupture in the Western segment (M_w 8.9) generates wave heights (~2.8 m) and current velocities (>2.0 m/s) at the Kooh Mobarak area that are comparable to those of a worst-case Central Makran scenario (M_w 9.0). Furthermore, a sensitivity analysis regarding the initial tidal level reveals a critical hydrodynamic dichotomy: while increasing the water level to Mean High Water Springs (MHWS) slightly attenuates the pure tsunami amplitude due to reduced non-linear shoaling, it significantly elevates the Total Water Level, thereby expanding the inundation extent into backshore tidal creeks. These findings underscore the imperative of adopting a dual-criterion design approach that incorporates near-field western ruptures and compound tidal interactions to ensure the resilience of critical coastal structures.

1. Introduction

The Makran Subduction Zone (MSZ), an extensive geological feature stretching approximately 900 km along the northern Arabian Sea, represents one of the most enigmatic and potentially hazardous tsunamigenic structures in the Indian Ocean basin. Formed by the northward subduction of the Arabian Plate beneath the Eurasian Plate at a rate of approximately 4 cm/year, the MSZ is characterized by an exceptionally thick accretionary wedge, sediments scraped off the subducting plate, which exceeds 7 km in thickness. This unique geological configuration distinguishes it from other well-studied subduction zones, such as the Japan Trench or the Sumatra-Andaman zone. While the seismic recurrence intervals in the Makran region are historically longer than those of the Pacific Ring of Fire, the geomorphological evidence suggests a capacity for generating mega-thrust earthquakes with magnitudes exceeding M_w 8.5 (Heidarzadeh et al., 2008; Smith et al., 2013). The catastrophic potential of this region was vividly demonstrated on November 28, 1945, when an M_w 8.1

earthquake occurred in the eastern segment of the MSZ. This event generated a trans-oceanic tsunami that devastated the coasts of Pakistan, Iran, Oman, and western India, claiming over 4,000 lives. Reports of run-up heights exceeding 12 meters in some localities, combined with the delayed arrival of the largest waves, have led researchers to hypothesize that the 1945 event was likely amplified by secondary submarine landslides triggered by the seismic shock (Okal and Synolakis, 2008; Rajendran et al., 2008). This historical precedent underscores a critical reality: despite the paucity of instrumental records compared to other subduction zones, the Makran coast is highly vulnerable to extreme hydrodynamic events.

From a tectonic perspective (Fig. 1), the MSZ is complex and heterogeneous. It is widely accepted in the scientific community that the zone is segmented into eastern and western blocks, separated roughly by the Sonne Fault or the Pol-Abneh interpretation structure (Kukowski et al., 2001). The eastern segment, located primarily offshore Pakistan, has been seismically active in recent history and is relatively well-documented in earthquake catalogs. Conversely, the western segment, extending offshore from the Iranian coast towards the Strait of Hormuz, has exhibited a distinct lack of large instrumental earthquakes over the past few centuries. This prolonged period of quiescence has created a prominent "seismic gap" (Byrne et al., 1992). This has led to significant debate regarding the frictional properties of the plate interface. Early hypotheses suggested that the western Makran might be behaving a seismically, releasing stress through stable sliding or "creep" due to the high-water content within the soft sediments. However, recent advancements in geodetic monitoring and thermal modeling have challenged this view. GPS measurements of coastal uplift and plate motion vectors strongly suggest that the plate interface in the western Makran is structurally coupled (locked) to a significant depth (Frohling and Szeliga, 2016; Penney and Copley, 2019). If this locking hypothesis holds true, the accumulated elastic strain over centuries could be released in a future mega-thrust earthquake with a magnitude comparable to, or exceeding, the 1945 event. Consequently, hazard assessments that focus solely on the historically active eastern segment, or assume the western segment is benign, may drastically underestimate the risk to the rapidly developing Iranian coast.

In the aftermath of the devastating 2004 Indian Ocean Tsunami, the scientific community intensified efforts to quantify the hazard in the northwestern Indian Ocean. Pioneering numerical studies by Heidarzadeh et al. (2008, 2009) provided the first systematic evaluation of historical and hypothetical tsunamis in the region. Their work was instrumental in establishing regional propagation patterns and verifying the source mechanisms of the 1945 event. Concurrently, field surveys and theoretical analyses by Okal and Synolakis (2008) highlighted the complexity of tsunami generation in the Makran, emphasizing the role of sedimentary features. More recently, El-Hussain et al. (2016) presented a comprehensive Probabilistic Tsunami Hazard Assessment (PTHA) for the coast of Oman, providing valuable return period estimates for various wave heights. Regarding the Iranian coastline, however, site-specific engineering studies have been geographically skewed. The majority of research has concentrated on the port of Chabahar and the eastern sectors, driven by the proximity to the 1945 rupture zone (Mokhtari, 2011; Rashidi et al., 2020). Furthermore, many of these regional studies utilized relatively coarse bathymetric grids, which are insufficient for resolving the complex wave-structure interactions in nearshore environments. As a result, the specific hydrodynamic risks to the westernmost extremity of the Makran zone, specifically the Kooh Mobarak region, remain poorly understood. This lack of detailed data is particularly concerning given the complex coastal morphology of the area, which includes tidal creeks (Khors) and shallow shelves that can significantly alter tsunami amplification factors.

In this study, Kooh Mobarak is selected as the case-study area due to ongoing marine-oriented development and the presence of diverse coastal and offshore infrastructure, including ports, breakwaters, jetties, energy-related facilities, and offshore loading and mooring systems. Unlike static coastal structures, offshore facilities are particularly sensitive not only to wave height (run-up) but also to current velocities. Strong tsunami-induced currents can exert substantial drag forces on moored vessels and subsea pipelines, potentially triggering operational failures or environmental impacts even when coastal inundation is moderate. Therefore, generic regional hazard maps may be insufficient for the design and safety assessment of such high-value assets, and high-resolution local modeling is warranted.

Another critical limitation in many existing deterministic assessments is the simplification of the background sea level. Most studies simulate tsunami run-up assuming Mean Sea Level (MSL) as a static datum. However, the Persian Gulf and the Gulf of Oman are characterized by a mixed semi-diurnal tidal regime with significant tidal ranges, often exceeding 2 meters. The interaction between a tsunami wave train and the astronomical tide is non-linear; the water depth modulation caused by tides affects the wave celerity, shoaling coefficients, and bottom friction dissipation (Kowalik and Proshutinsky, 2010). Neglecting the High-Water Spring (MHWS) condition, effectively the "worst-case" hydraulic scenario, can lead to a dangerous underestimation of the maximum inundation limit and the total water level required for determining the crest elevation of coastal defense structures. Conversely, ignoring low-tide conditions might

underestimate the current velocities induced by the receding drawdown.

To address these knowledge gaps and provide a robust basis for engineering design, this study presents a comprehensive, high-resolution deterministic tsunami hazard assessment for the Kooh Mobarak coastal area. By employing the ComMIT/MOST (Method of Splitting Tsunami) numerical model within a system of dynamically nested grids, we achieve the spatial resolution necessary to capture nearshore hydrodynamic phenomena. Twelve distinct fault rupture scenarios were defined and simulated, covering the western, central, and eastern segments of the Makran Subduction Zone, with magnitudes ranging from M_w 8.0 to 9.0. This study distinguishes itself from previous works through three primary contributions: First, it rigorously evaluates the "Western Gap" hypothesis by quantifying the specific impact of a western Makran rupture on Kooh Mobarak, challenging the conventional focus on the east. Second, it moves beyond simple wave height analysis to provide detailed maps of current velocities, which are essential for the integrity of offshore and nearshore structures. Third, it performs a sensitivity analysis on the initial tidal level, explicitly comparing simulations at MSL and MHWS to determine the compound risk and establish conservative design criteria for coastal resilience.

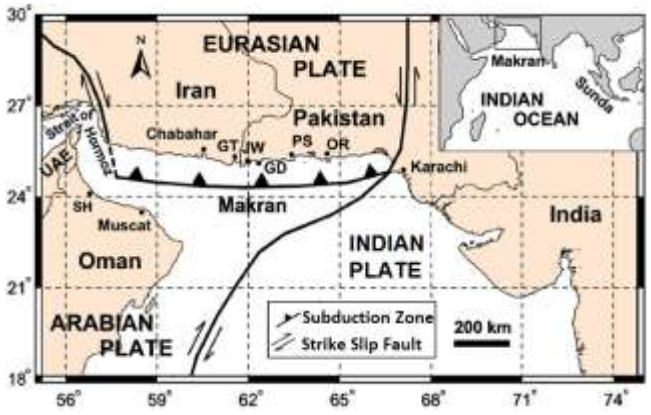

Figure 1. Tectonic map of the Makran Subduction Zone in the northwestern Indian Ocean (Heidarzadeh et al., 2009)

2. Tectonic Setting and Source Characterization

The Makran Subduction Zone (MSZ) constitutes the active boundary between the converging Arabian and Eurasian plates. This structure extends for nearly 900 km from the transpressive Ornach-Nal fault system in the east (Pakistan) to the Minab-Zendan fault system in the west (Iran). Geodetic measurements indicate that the Arabian oceanic lithosphere is subducting beneath the continental Eurasian plate at a rate of approximately 19.5 mm/yr near the eastern boundary, increasing to roughly 27 mm/yr towards the west (Vernant et al., 2004). A defining characteristic of the MSZ is its exceptionally thick accretionary prism, resulting from the immense sediment input from the Himalayas and the Zagros Mountains. This sedimentary wedge, exceeding 7 km in thickness, coupled with a very shallow dip angle of the subducting slab (typically less than 10°), creates a geometric configuration highly favorable for the generation of large-magnitude tsunamigenic earthquakes (Smith et al., 2013). The low dip angle implies a wider seismogenic zone, allowing for rupture propagation over a larger area, which directly correlates with the volume of water displaced during a seismic event.

2.1. Segmentation and Seismicity

Although the MSZ appears as a continuous feature, seismic activity is non-uniform along its strike. Tectonically, the zone is segmented into eastern and western blocks, likely separated by the Sonne Fault or a similar transverse structure near 60.5°E (Kukowski et al., 2001). The eastern segment has demonstrated its potential for mega-thrust events, most notably the 1945 M_w 8.1 earthquake. In contrast, the western segment, situated directly offshore of the Kooh Mobarak region and the Strait of Hormuz, has historically been inactive. However, the absence of recent large earthquakes does not imply safety. Recent elastic block modeling and GPS data analysis suggest that the western Makran is significantly locked, accumulating strain that could be released in a future event with a magnitude exceeding M_w 8.5 (Frohling and Szeliga, 2016).

To address this hazard heterogeneity, this study adopts a segmented approach. As illustrated in Figure 2, the MSZ is divided into three distinct rupture zones: the Western Makran, the Central Makran, and the Eastern Makran. This segmentation allows for the definition of independent rupture scenarios, ensuring that the specific threat to the Kooh Mobarak from the adjacent western segment is isolated and quantified, rather than being averaged out in a whole-margin model.

2.2. Deterministic Source Modeling

Given the lack of high-resolution precursor data for future earthquakes in the region, a deterministic approach based on the "characteristic earthquake" model was employed. The tsunami sources were modeled as rectangular fault planes embedded in an elastic half-space, following the standard dislocation theory proposed by Okada (1985). This analytical model calculates the vertical seafloor deformation, uplift and subsidence, which is then translated instantaneously to the sea surface to form the initial tsunami wave condition.

To accurately represent the curvilinear geometry of the Makran trench, the fault interface was discretized into a grid of 20 rectangular unit sources (sub-faults), arranged in two parallel rows aligned with the trench strike. As depicted in Figure 3, the 'a-series' represents the shallow updip interface (closer to the trench), while

the 'b-series' corresponds to the deeper downdip interface. The geometric parameters for these unit sources, including strike, dip, and depth, were adopted from the seismotectonic model of Heidarzadeh et al.

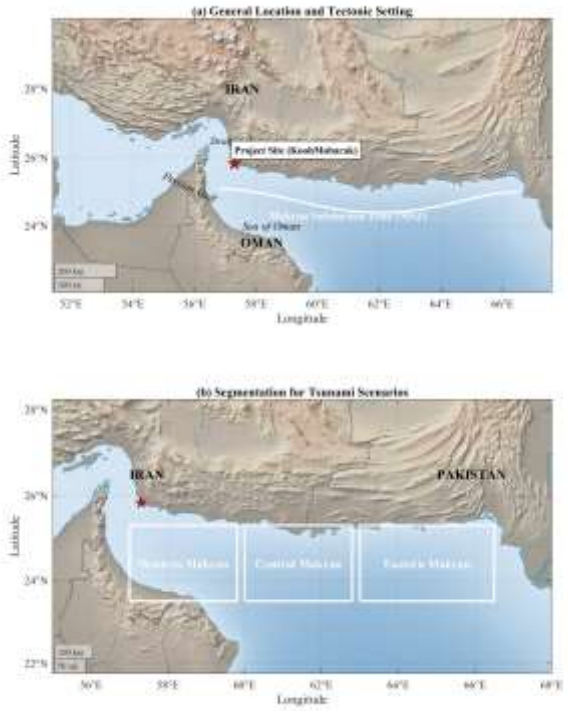

Figure 2. (a) General tectonic setting of the northwestern Indian Ocean, illustrating the trace of the Makran Subduction Zone (MSZ) deformation front (white line) relative to the Kooh Mobarak (red star) near the Strait of Hormuz. (b) Segmentation of the MSZ into Western, Central, and Eastern sectors. The white rectangles delineate the surface projection of the source areas used to define the deterministic fault rupture scenarios for tsunami modeling in this study.

(2009). The shallow sub-faults were modeled with a dip angle of 3◦ and a centroid depth of roughly 5–7 km, while the deeper row utilized a dip of 3◦ but at a greater depth, reflecting the gentle subduction angle. The strike angles were adjusted along the trench curvature, ranging from approximately 237◦ in the west to 297◦ in the east. A uniform rake angle of 90∘ (pure thrust) was assumed for all segments to maximize the vertical seafloor displacement, representing a conservative "worst-case" assumption for tsunami generation.

3. Methodology

The numerical simulation of tsunami generation, propagation, and coastal inundation is a complex multi-scale problem that requires a robust hydrodynamic framework. To accurately capture the physics of tsunami waves from the deep ocean to the shallow coastal waters of Kooh Mobarak, this study utilizes the ComMIT/MOST system (Community Model Interface for Tsunami / Method of Splitting Tsunami). Developed by the Pacific Marine Environmental Laboratory (PMEL) of NOAA, this model has been extensively validated against laboratory benchmarks and historical field data, including the 2004 Indian Ocean and 2011 Tohoku tsunamis (Titov and Gonzalez, 1997; Titov et al., 2011). The methodology employed in this study comprises four integral components: the mathematical formulation of the hydrodynamic equations, the integration of high-resolution bathymetric and topographic data, the establishment of a nested grid system, and the definition of rupture scenarios.

3.1. Governing Equations and Numerical Scheme

Tsunamis generated by submarine earthquakes are characterized by wavelengths that are significantly larger than the water depth ($L \gg h$). Consequently, their dynamics are governed by the Nonlinear Shallow Water Equations (NSWE). The MOST model solves these equations in spherical coordinates to account for the Earth's curvature, which is essential for accurate propagation over the large distances involved in the Makran Subduction Zone. The governing continuity and momentum equations are expressed as follows:

$$\frac{\partial h}{\partial t} + \frac{1}{R\cos\phi}\left[\frac{\partial (uh)}{\partial \lambda} + \frac{\partial (vh\cos\phi)}{\partial \phi}\right] = 0 \quad (1)$$

$$\frac{\partial u}{\partial t} + \frac{u}{R\cos\phi}\frac{\partial u}{\partial \lambda} + \frac{v}{R}\frac{\partial u}{\partial \phi} + \frac{g}{R\cos\phi}\frac{\partial \eta}{\partial \lambda} = fv - \frac{gn^2 u\sqrt{u^2+v^2}}{h^{4/3}} \quad (2)$$

$$\frac{\partial v}{\partial t} + \frac{u}{R\cos\phi}\frac{\partial v}{\partial \lambda} + \frac{v}{R}\frac{\partial v}{\partial \phi} + \frac{g}{R}\frac{\partial \eta}{\partial \phi} = -fu - \frac{gn^2 v\sqrt{u^2+v^2}}{h^{4/3}} \quad (3)$$

where λ and ϕ represent longitude and latitude, respectively; R is the Earth's radius; t is time; $h=\eta + d$ is the total water depth (η is the wave surface elevation and d is the undisturbed water depth); u and v are the depth-averaged zonal and meridional velocity components; g is the gravitational acceleration; and f is the Coriolis parameter. The term containing n represents the bottom friction, parameterized using the Manning roughness coefficient. The numerical solution employs the method of fractional steps, or "splitting," which discretizes the spatial derivatives using a finite-difference scheme. This approach separates the governing equations into two one-dimensional systems (along the λ and ϕ axes), which are solved sequentially. This technique significantly reduces computational cost while maintaining numerical stability and minimizing numerical dispersion, making it highly suitable for operational tsunami forecasting and hazard assessment (Titov and Synolakis, 1998).

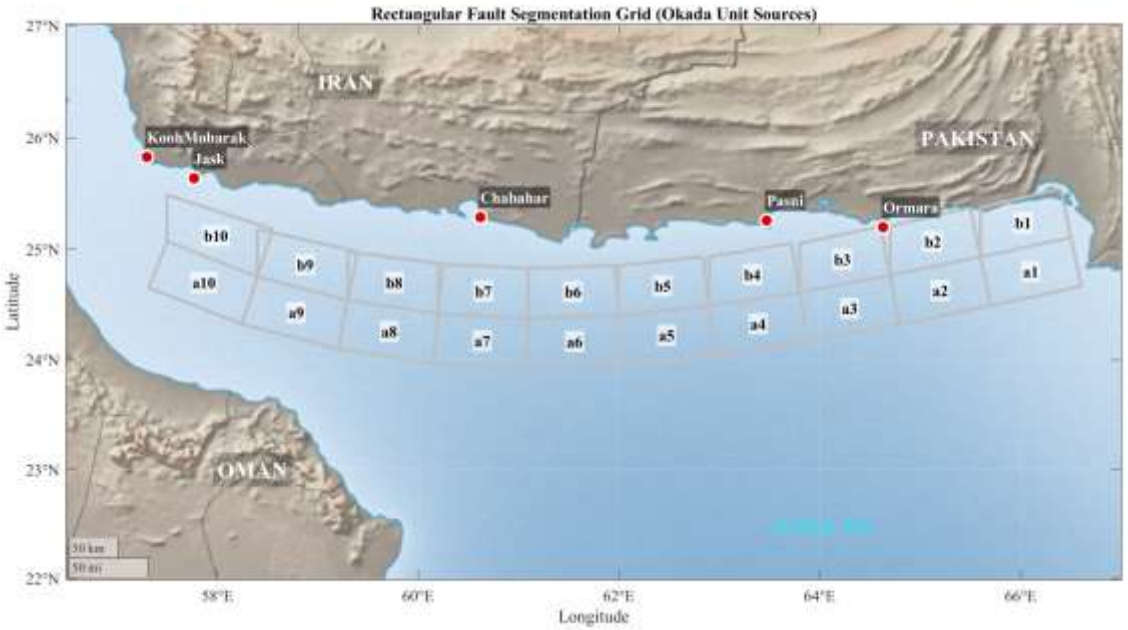

Figure 3. Spatial configuration of the rectangular unit sources (sub-faults) used for the deterministic tsunami modeling. The grid comprises two parallel rows aligned with the strike of the Makran Subduction Zone: the 'a-series' represents the shallow up-dip interface, and the 'b-series' corresponds to the deeper down-dip interface. Key coastal locations, including the study site at Kooh Mobarak, are marked for reference

3.2. Bathymetric and Topographic Data Integration

The accuracy of nearshore tsunami modeling is heavily dependent on the quality of the Digital Elevation Model (DEM). For this study, a seamless DEM was constructed by merging multiple datasets. For the deep ocean and regional propagation areas, bathymetric data were derived from the GECO 30 arc-second grid. For the nearshore and inundation zones, high-resolution topographic data from the Shuttle Radar Topography Mission (SRTM) were integrated with local hydrographic survey data. All datasets were referenced to the Mean Sea Level (MSL) for the baseline simulations. For the sensitivity analysis regarding tidal effects, the bathymetry was dynamically adjusted to represent the Mean High-Water Springs (MHWS) level, effectively increasing the water depth by approximately 1.03 meters relative to MSL in the domain, based on local tidal constituents (Kowalik and Proshutinsky, 2010).

3.3. Nested Grid System and Boundary Conditions

To bridge the scale gap between the trans-oceanic propagation (hundreds of kilometers) and the local inundation at the Kooh Mobarak (tens of meters), a system of three dynamically coupled nested grids was developed, as illustrated in Figure 4. The outermost grid (Grid A) covers the entire Northern Indian Ocean and the Makran Subduction Zone with a resolution of 2 arc-minutes (approx. 3.6 km). This grid captures the source generation and the initial directivity of the tsunami energy. The intermediate grid (Grid B), nested within Grid A, focuses on the Gulf of Oman and the entrance to the Strait of Hormuz with a resolution of 30 arc-seconds (approx. 900 m). This refinement is crucial for resolving the wave transformation as it enters the continental shelf. Finally, the innermost grid (Grid C) covers the Kooh Mobarak coastal area, and the adjacent tidal creeks with a high resolution of 3 arc-seconds (approx. 90 m). This fine resolution allows the model to explicitly resolve the interaction of tsunami waves with nearshore structures and to accurately simulate the run-up process on land.

The model utilizes a "moving boundary" condition at the shoreline to simulate inundation. In the wet cells, the governing equations are solved as described, while in the dry cells (land), the water depth is zero. As the wave propagates, the interface between wet and dry cells is updated at each time step, allowing the water to flood onto the topography. To account for energy dissipation due to bottom roughness in the nearshore and overland flow, a constant Manning's roughness coefficient of n=0.025 $m^{-1/3}s$ was applied uniformly across Grid C. This value is consistent with recommended standards for coastal terrains characterized by mixtures of sand, mud, and sparse vegetation (ASCE, 2017; Kotani et al., 1998). The simulation duration was set to 6 hours for each scenario to ensure that not only the first wave but also subsequent resonant waves and edge waves were captured.

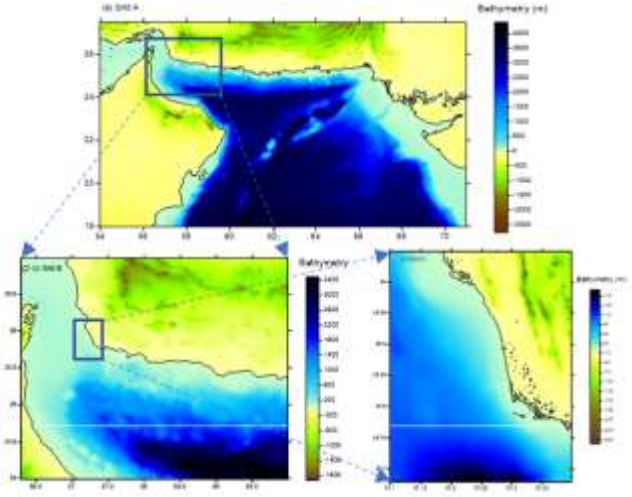

Figure 4. Configuration of the nested bathymetric and topographic grid system used for the numerical simulation. (a) Regional Grid A covers the entire Makran Subduction Zone to capture tsunami generation; (b) Intermediate Grid B focuses on wave propagation into the Gulf of Oman and the Strait of Hormuz; and (c) High-resolution local Grid C targets the Kooh Mobarak coastal area to resolve nearshore hydrodynamics and potential inundation zones.

3.4. Scenario Definition

To systematically investigate the tsunami hazard, a suite of twelve deterministic fault rupture scenarios was defined, covering a comprehensive range of magnitudes and locations. As detailed in Table 1, the scenarios are categorized based on their rupture location within the three tectonic segments identified in Section 2: Western, Central, and Eastern Makran. For each segment, four distinct moment magnitudes (M_w) were simulated: 8.0, 8.4, 8.7, and 8.9. In addition, a "worst-case" scenario of M_w 9.0, assuming a full-margin rupture, was simulated in the Central Makran as a benchmark for maximum credible event analysis.

To ensure that the modeled events are physically consistent with global earthquake databases, the geometric fault parameters for each scenario, specifically rupture length (L), width (W), and average slip (u) were derived from the empirical scaling laws of Wells and Coppersmith (1994). These relationships relate the moment magnitude (M_w) to the fault dimensions as follows:

$$\text{Log } (L) = -3.22+0.69M_w \quad (4)$$

$$\text{Log } (W) = -1.01+0.32\text{Mw} \quad (5)$$

$$\text{Log } (u) = -4.80+0.69M_w \quad (6)$$

Based on these equations, the rupture scenarios were constructed by activating specific combinations of the unit sources defined in Figure 3. For instance, an M_w 8.0 event typically involves a rupture length of approximately 200 km, activating roughly 4 adjacent unit sources, while the extreme M_w 9.0 scenario assumes a rupture length exceeding 900 km, activating the entire interface. The recurrence periods associated with these magnitudes, also listed in Table 1, were adopted from El-Hussain et al. (2016) to provide temporal context for the hazard, ranging from ~125 years for smaller events to ~950 years for the catastrophic scenarios. This structured approach allows for a direct comparison of the hydrodynamic impact based on both the magnitude and the geographical origin of the tsunami.

4. Results and Discussion

This section presents a comprehensive and multi-scalar analysis of the deterministic tsunami simulations, systematically integrating findings from the regional propagation patterns down to the localized hydrodynamics close to the Kooh Mobarak area. The discussion is structured to first elucidate the spatiotemporal evolution of the wave train and its directivity across the nested grid system, providing insights into arrival times and near-field characteristics. Subsequently, the analysis zooms in to the nearshore domain to quantify the critical engineering parameters, specifically maximum wave surface elevations and current velocities, at 3 monitoring stations. Beyond the absolute quantification of hazard, this section rigorously examines the physical sensitivity of the coastal response to source rupture parameters, exploring scaling laws and hydrodynamic correlations to validate the model's consistency. Finally, to address the compound nature of the risk in this macrotidal region, the non-linear interaction between the tsunami surge and astronomical tides is evaluated, defining the "worst-case" hydraulic scenarios for structural design and inundation mapping.

4.1. Spatiotemporal Propagation and Spatial Distribution

The hydrodynamic evolution of the generated tsunamis is fundamentally governed by the interplay between the seismic source mechanism, specifically the fault strike and rake, and the regional bathymetric configuration of the Oman Basin. Figure 5 illustrates the spatiotemporal propagation of the wave train for the worst-case Central Makran scenario (M9.0-C) across the nested grid system. A dominant feature observed in the regional field (Figure 5a) is the pronounced directivity of the radiated energy. Consistent with the classic hydrodynamics of elongated sources, the primary energy beam is directed orthogonally to the main axis of the rupture zone. Given the east-west orientation of the Makran trench, this results in a bi-directional propagation pattern: a southward wavefront propagating into the deep Arabian Sea and a northward

Table 1. Tsunami modeling scenarios defined based on earthquake magnitude, recurrence interval, and associated fault source parameters along the Makran Subduction Zone.

Magnitude (Mw)	Return Period (Tr)	Slip (u) [m]	Length (L) [km]	Width (W) [km]	Rupture Location	Scenario ID
8.0	125	4.0	200	50	Western Makran	M8.0-W
					Central Makran	M8.0-C
					Eastern Makran	M8.0-E
8.4	266	10.0	300	50	Western Makran	M8.4-W
					Central Makran	M8.4-C
					Eastern Makran	M8.4-E
8.7	486	17.0	500	50	Western Makran	M8.7-W
					Central Makran	M8.7-C
					Eastern Makran	M8.7-E
8.9	750	23.0	700	50	Western Makran	M8.9-W
					Eastern Makran	M8.9-E
9.0	946	27.0	900	50	Central Makran	M9.0-C

* Return periods are adopted from El-Hussain et al. (2016).

wavefront advancing directly towards the Iranian and Pakistani coastlines.

For the Kooh Mobarak region, situated at the westernmost extremity of the MSZ near the Strait of Hormuz, this directivity has critical implications. Unlike tsunamis originating from the Eastern Makran segment (offshore Pakistan), which must travel parallel to the continental shelf and undergo significant diffraction, geometric spreading, and scattering around coastal promontories, waves generated by the Western and Central segments propagate almost directly upslope towards the Kooh Mobarak shelf. This direct path minimizes energy attenuation, allowing the wave train to retain a substantial portion of its initial energy upon reaching the continental slope. The time-series analysis of the free surface elevation reveals that the leading wave reaches the Kooh Mobarak coastline approximately 33 to 45 minutes post-rupture (Figure 5c). This rapid arrival time unequivocally classifies the event as a local, near-field tsunami, leaving a minimal temporal window for evacuation and rendering distant regional warning centers less effective for this specific locale. Furthermore, the simulation indicates that for certain rupture scenarios, the initial arrival manifests as a leading depression wave (sea-level drawdown) prior to the arrival of the massive crest, a phenomenon often associated with the landward side of subduction zone uplifts.

Upon entering the shallow coastal waters (Grid C), the wave dynamics transition from linear propagation to non-linear transformation. Figure 6 presents the spatial distribution of the maximum hydrodynamic parameters, providing insight into the wave-structure interaction. The maximum surface elevation map (Figure 6a) highlights a distinct non-uniformity in run-up distribution. We observe localized energy focusing around the coastal headlands. This amplification is attributed to the convergence of wave orthogonal caused by refraction over the convex bathymetric contours of the headland (the "cape effect"). Consequently, the wave height at the tip of the breakwater and adjacent protrusions is significantly higher than along the straight sections of the coastline.

The hydrodynamic hazard is further elucidated by the maximum velocity map (Figure 6b). While offshore velocities are relatively low (< 0.5 m/s), the simulation reveals zones of intense flow acceleration in the nearshore region. Most notably, velocities exceeding 2.0 m/s are concentrated at ST3 station in water depth of 10 m. This acceleration is driven by two physical mechanisms: first, the conservation of mass requiring flow acceleration as the water depth decreases (shoaling); and second, the flow constriction and lateral separation of the flow as it bypasses the any obstructions. These high-velocity jets are of particular engineering concern, as they can induce severe scour at the toe of the breakwater and exert substantial hydrodynamic drag forces on vessels traversing the channel, potentially compromising navigation safety during the event.

4.2. Comparative Analysis of Rupture Scenarios and Hydrodynamic Amplification

To rigorously quantify the variability of the tsunami hazard relative to the seismic source characteristics, the maximum hydrodynamic parameters, specifically wave height (H_{max}) and current velocity (V_{max}), were extracted at three monitoring stations, including ST1 and ST2 located in the offshore domain (water depth ~40–50 m), and ST3 situated in the nearshore zone (water depth ~10 m).

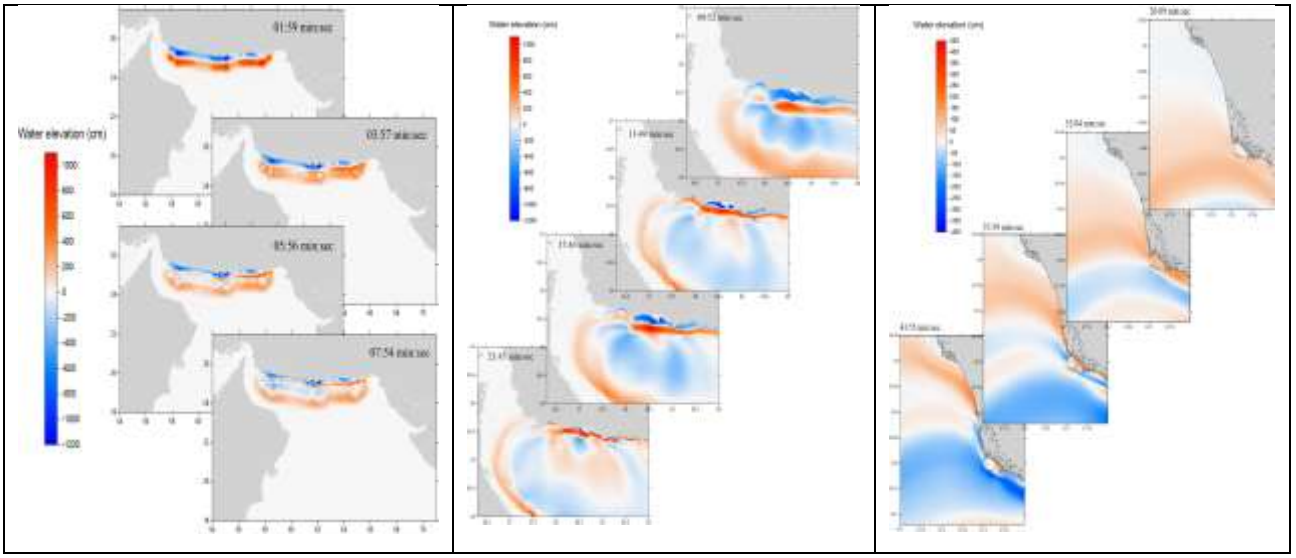

Figure 5. Spatiotemporal evolution of tsunami wave propagation for the worst-case Central Makran scenario (M9.0-C) across the nested grid system. (a) Regional propagation in Grid A, illustrating the initial generation and N-NW directivity of the wave energy; (b) Intermediate wave dynamics in Grid B, showing the wave train traversing the Gulf of Oman towards the Strait of Hormuz; and (c) Nearshore propagation and initial impact in Grid C, depicting the wave shoaling process and the arrival of the leading wave at the Kooh Mobarak coastline approximately 30–45 minutes post-rupture.

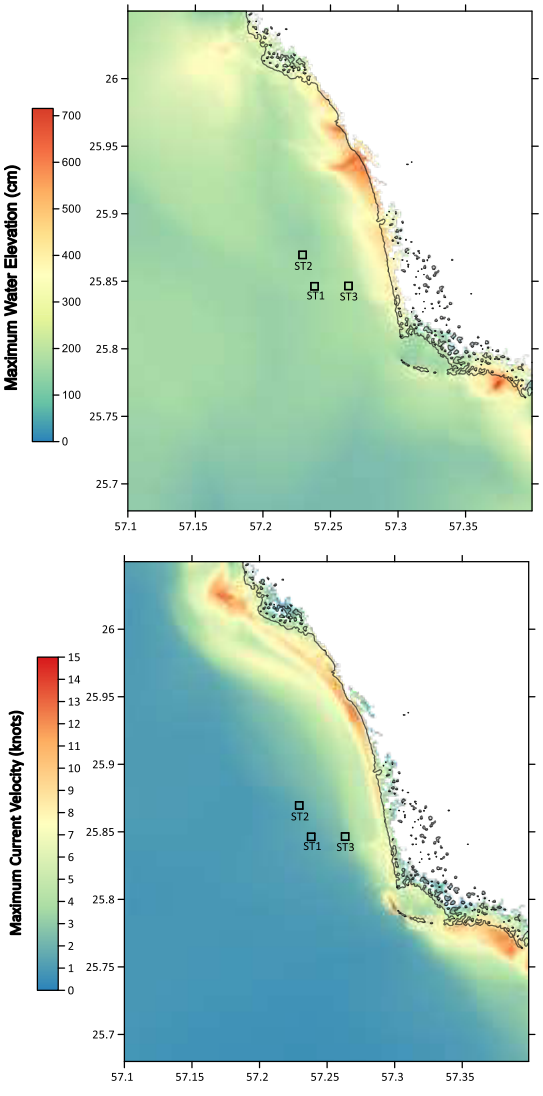

Figure 6. Spatial distribution of peak hydrodynamic parameters simulated for the worst-case Central Makran scenario (M9.0-C) within the high-resolution local grid. (a) Maximum wave surface elevation, indicating the potential run-up limit along the Kooh Mobarak coastline; and (b) Maximum tsunami-induced current velocity, highlighting areas of intense flow acceleration, particularly near the ST3 monitoring station.

Figure 7 presents a comparative analysis of H_{max} across the twelve fault rupture scenarios. A cross-examination of the data reveals a profound bathymetric amplification. While the offshore stations experience moderate wave heights (typically 1.5–1.7 m for extreme scenarios), the wave height amplifies by a factor of nearly two as it propagates to the nearshore station (ST 3). This behavior is consistent with the principle of energy flux conservation under Green's Law ($H \propto h^{-1/4}$); as the tsunami wave train enters shallower waters, the decrease in celerity necessitates an increase in amplitude to conserve energy flux, resulting in the steepening of the wave front before impact.

A pivotal finding of this study emerges from the comparison of source scenarios. Conventionally, tsunami hazard is assumed to scale linearly with earthquake magnitude (M_w). However, our results challenge this assumption for the Kooh Mobarak region. While the Central Makran scenario (M9.0-C) produces the absolute peak wave height (H_{max}=2.92m), the Western Makran scenario (M8.9-W) generates a comparable amplitude of 2.79 m at ST 3, a difference of less than 5%. This observation underscores the critical role of source proximity over pure magnitude.

Waves generated by the Central or Eastern segments must traverse a significant distance across the shelf, undergoing geometric spreading and frequency dispersion, which attenuates their energy density before reaching Kooh Mobarak. In contrast, the Western segment acts as a near-field source; the wave energy is radiated directly onto the local shelf with minimal distance-induced attenuation. Consequently, the "Western Gap," often considered less critical due to its seismic quiescence, poses a hydrodynamic threat virtually equivalent to a full-scale rupture of the Central Makran zone.

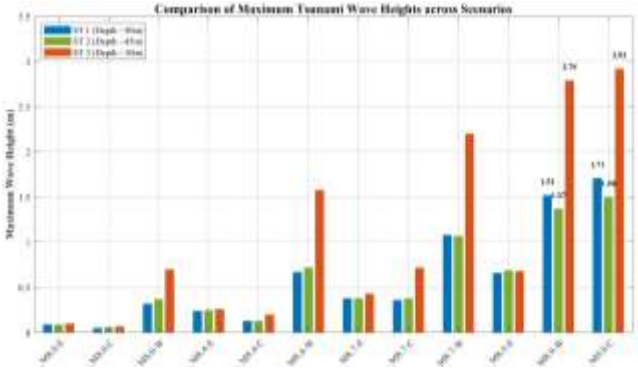

Figure 7. Comparative analysis of maximum tsunami wave heights recorded at offshore Stations (ST 1 and ST 2) and the nearshore Station (ST 3) across twelve fault rupture scenarios. The results highlight significant wave amplification at the ST 3 due to shoaling effects in shallower waters (~10 m depth). Notably, the Western Makran scenario (M8.9-W) generates wave heights comparable to the worst-case Central scenario (M9.0-C), emphasizing the critical hazard posed by the western segment despite its slightly lower magnitude.

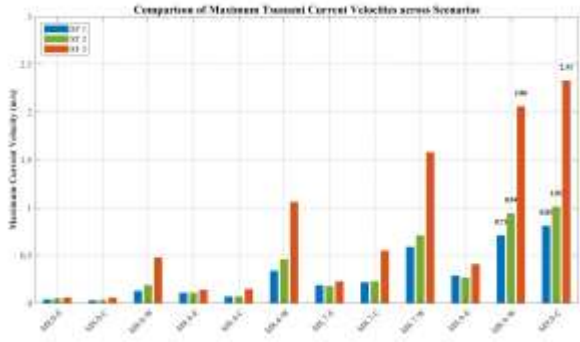

Figure 8. Maximum tsunami-induced current velocities at key marine facility locations for different seismic scenarios. The ST3 experiences the most severe hydrodynamic conditions, with velocities exceeding 2.0 m/s in the extreme scenarios (M8.9-W and M9.0-C). This sharp increase in velocity near the coast, relative to the offshore STs, indicates strong flow acceleration driven by the bathymetric gradient and coastal constriction.

The analysis of flow dynamics, presented in Figure 8, further elucidates the hazard profile. The results indicate a transition from a potential-energy-dominated regime offshore to a kinetic-energy-dominated regime nearshore. At the offshore stations, current velocities remain relatively moderate (< 1.0 m/s), even for the largest events. However, at station ST3, velocities exhibit a sharp, non-linear increase, exceeding 2.3 m/s for the M9.0-C scenario and 2.0 m/s for the M8.9-W scenario. This intensification is driven by the conversion of potential energy into kinetic energy as the wave shoals compounded by bottom friction. From an engineering perspective, current velocities of this magnitude are capable of exerting immense hydrodynamic drag forces ($F_D \propto V^2$) on moored vessels and can initiate rapid scour around the toe of marine structures. Therefore, coastal protection designs for Kooh Mobarak must not only account for the static pressure of the run-up elevation but also the dynamic pressure induced by these high-velocity sustained flows.

4.3. Hazard Scaling and Hydrodynamic Correlations

To elucidate the underlying physics of the hazard and the sensitivity of the coastal response to source parameters, Figure 9 presents the scaling relationship between the earthquake magnitude (M_w) and the maximum wave height at ST3 location. The plotted curves reveal a critical insight into the hazard sensitivity gradient. The response curve for the Western segment (orange line) exhibits a highly non-linear, exponential-like growth. This implies that the Kooh Mobarak coastline is "hypersensitive" to ruptures in this sector; a seemingly distinct increase in magnitude (e.g., from M_w 8.4 to 8.7) results in a disproportionate, multi-fold amplification of the wave height. This steep gradient is attributed to the lack of geometric attenuation; since the source is in the near-field, the radiated energy flux impinges directly on the coast without significant dispersion. In sharp contrast, the Eastern segment (blue line) displays a flat, asymptotic response. Even for a massive M_w 8.9 event in the east, the wave height at Kooh Mobarak remains minimal. This confirms that the region is effectively "shielded" from eastern ruptures by a combination of large propagation distances (~500 km) and the unfavorable orientation of wave orthogonals relative to the coastline.

Furthermore, the internal consistency of the numerical model is corroborated by the hydrodynamic correlation analysis presented in Figure 10, which maps the relationship between maximum current velocity (V_{max}) and wave height (H_{max}) across all simulated scenarios. The plotted data points distinctly segregate into two physical regimes based on local bathymetry. In the deep-water domain (ST1 and ST2 stations, depth ~40-50 m), the data form a cohesive "Offshore Regime" characterized by a quasi-linear relationship with a low slope. This behavior aligns well with linear wave theory, where orbital velocities remain relatively small compared to the wave celerity. In stark contrast, the

data collected at the ST3 station (depth ~10 m) define a "Nearshore Regime" that follows a strong power-law distribution ($V \propto H^k$, with $R^2>0.9$). This non-linear scaling indicates that as the wave enters shallow water, the conversion of potential energy into kinetic energy accelerates, confirming that the model correctly captures the non-linear advection processes that become dominant in the nearshore zone.

The dashed line in Figure 10 represents this power-law fit, validating that the model correctly captures the non-linear advection terms in the shallow water equations. From a design perspective, this correlation is pivotal; it demonstrates that in the shallow approach channel, a marginal increase in wave height (e.g., due to a slightly larger earthquake or tide) will translate into a substantial increase in current velocity. Consequently, the design of scour protection systems must be robust enough to withstand these disproportionately high kinetic loads, which scale non-linearly with the design wave height.

The dashed line in Figure 10 represents this power-law fit, validating that the model correctly captures the non-linear advection terms in the shallow water equations. From a design perspective, this correlation is pivotal; it demonstrates that in the shallow approach channel, a marginal increase in wave height (e.g., due to a slightly larger earthquake or tide) will translate into a substantial increase in current velocity. Consequently, the design of scour protection systems must be robust enough to withstand these disproportionately high kinetic loads, which scale non-linearly with the design wave height.

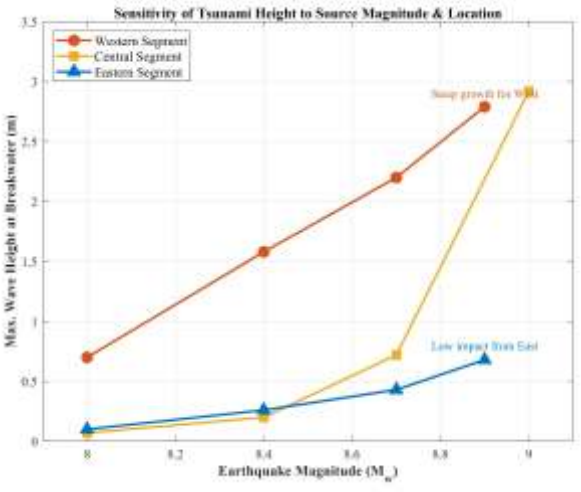

Figure 9. Sensitivity analysis of maximum tsunami wave height at the Kooh Mobarak with respect to earthquake magnitude (*Mw*) and rupture location. The steep gradient observed for the Western and Central segments (orange and yellow lines) contrasts with the negligible impact of the Eastern segment (blue line), highlighting the critical role of wave directivity and source proximity.

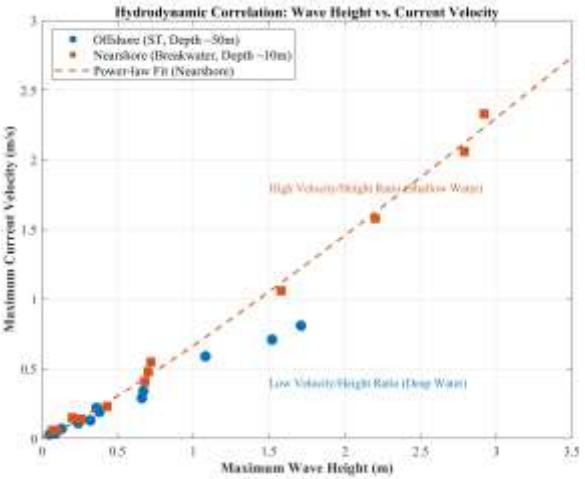

Figure 10. Hydrodynamic correlation between maximum current velocity and wave height across all simulated scenarios. The clear separation between offshore (ST1 , ST2, depth ~50 m) and nearshore (ST3, depth ~10 m) data points illustrates the non-linear amplification of currents due to shoaling effects. The dashed line represents a power-law fit for the nearshore data, validating the physical consistency of the model results.

4.4. Tidal Sensitivity Analysis and Compound Inundation Risk

Given the macrotidal regime of the Persian Gulf and the Gulf of Oman, where tidal ranges can exceed 2.0 meters, relying solely on Mean Sea Level (MSL) simulations may yield an incomplete picture of the hazard. To address this, a dedicated sensitivity analysis was conducted to evaluate the non-linear interaction between the tsunami wave train and the background astronomical tide. The worst-case seismic scenario (M9.0-C) was simulated under two distinct initial water level conditions: Mean Sea Level (MSL, +1.81 m CD) and Mean High Water Springs (MHWS, +2.84 m CD).

Figure 11 presents the hydrodynamic response at the monitoring stations, highlighting a consistent attenuation of tsunami amplitude with increased water depth. Despite being counter-intuitive, raising the level to MHWS reduces the maximum wave height at the ST3 location by ~15% (dropping to 2.48 m compared to 2.92 m at MSL).This reduction is fundamentally attributed to the depth-dependence of wave amplification dynamics described by Green's Law ($H \propto h^{-1/4}$) and the modulation of bottom friction. During high tide, the increased local water depth (h) reduces the non-linear shoaling coefficient, effectively dampening the steepening process of the wave front as it approaches the coast. Similarly, current velocities

show a slight reduction due to the larger cross-sectional area available for flow conveyance.

However, this attenuation in wave amplitude must not be misinterpreted as a reduction in the overall flood risk. The governing parameter for coastal inundation, run-up, and overtopping is the Total Water Level (TWL), defined as the superposition of the astronomical tide and the tsunami surge ($TWL=\eta_{tide}+\eta_{tsunami}$). In the MHWS scenario, despite the smaller tsunami component, the elevated baseline results in a TWL of approximately +5.32 m CD, which is significantly higher than the TWL observed in the MSL scenario (~+4.7 m CD).

Complementing the wave height analysis, Figure 11 illustrates the sensitivity of tsunami-induced current velocities to the initial tidal level. Consistent with the wave amplitude attenuation, a universal reduction in current velocity is observed under the high tide (MHWS) condition compared to MSL. For instance, at ST2 station, the maximum velocity decreases by 12.9% (from 1.01 m/s to 0.88 m/s). This reduction is hydraulically consistent with the conservation of mass; the increased water depth during MHWS provides a larger cross-sectional area for flow conveyance, thereby reducing the depth-averaged velocity required to transport the tsunami momentum flux.

However, the response is spatially non-uniform. At ST3 location, the sensitivity is markedly lower, showing only a 3.0% reduction (from 2.33 m/s to 2.26 m/s). This suggests that in the extremely shallow and restricted zone, the flow dynamics are dominated by local geometric constraints and strong non-linear advection, rendering them less sensitive to the background tidal depth variations compared to the deeper offshore stations.

This finding establishes a critical approach for engineering design. While the MHWS scenario governs the flood risk (due to higher run-up), the MSL scenario governs the hydrodynamic loads. Since drag forces on moored vessels and shear stresses on the seabed scale with the square of the velocity ($F_D \propto V^2$ and $\tau_b \propto V^2$), the MSL condition represents the "worst-case" for designing mooring systems and scour protection aprons. Therefore, neglecting the lower tidal levels in simulations could lead to an underestimation of the forces acting on the subsea infrastructure.

The implications of this compound hazard are visually demonstrated in the inundation maps shown in Figure 12. Comparing the inundation extents reveals that the MHWS condition significantly alters the hydraulic connectivity of the coastal zone. The higher baseline allows the tsunami surge to override coastal berms and natural barriers that would otherwise block the flow at MSL. Consequently, the inundation zone penetrates significantly deeper inland, particularly within the tidal creeks (Khors). As depicted by the expanded +4.5 m contour in Figure 12b, the MHWS scenario exposes critical backshore areas to flooding that remain dry under MSL simulations.

Therefore, for future engineering design in this area, a dual-criterion approach is strongly recommended. The MHWS scenario represents the critical case for determining the crest elevation of coastal structures and flood defense walls to prevent overtopping. Conversely, the MSL scenario, which generates slightly higher particle velocities due to shallower depths, represents the governing case for designing scour protection systems and calculating drag loads on submerged structures. Ignoring this tidal variability could lead to designs that are either vulnerable to overtopping during high tides or susceptible to erosion during lower tidal stages.

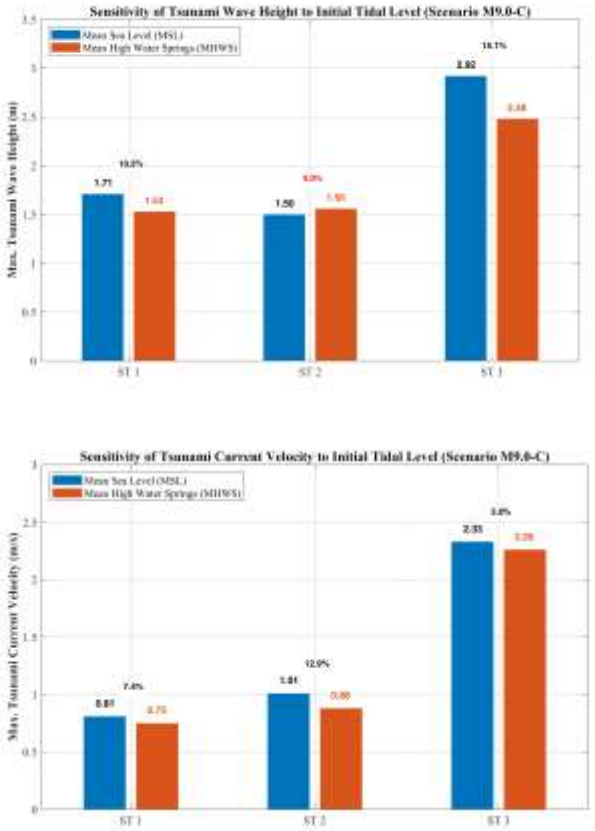

Figure 11. Sensitivity analysis of peak tsunami hydrodynamic parameters to initial tidal conditions for the worst-case Central Makran scenario (M9.0-C). (a) Maximum tsunami wave height; and (b) Maximum current velocity recorded at offshore (ST 1 and ST 2) and nearshore (ST 3) stations. Blue and orange bars denote simulations initialized at Mean Sea Level (MSL) and Mean High Water Springs (MHWS), respectively, with annotated values indicating the percentage variation. The observed attenuation of the pure tsunami amplitude and velocity during high tide (MHWS), particularly at ST3 location (~15% reduction in height), is attributed to the reduced non-linear shoaling amplification resulting from the increased local water depth.

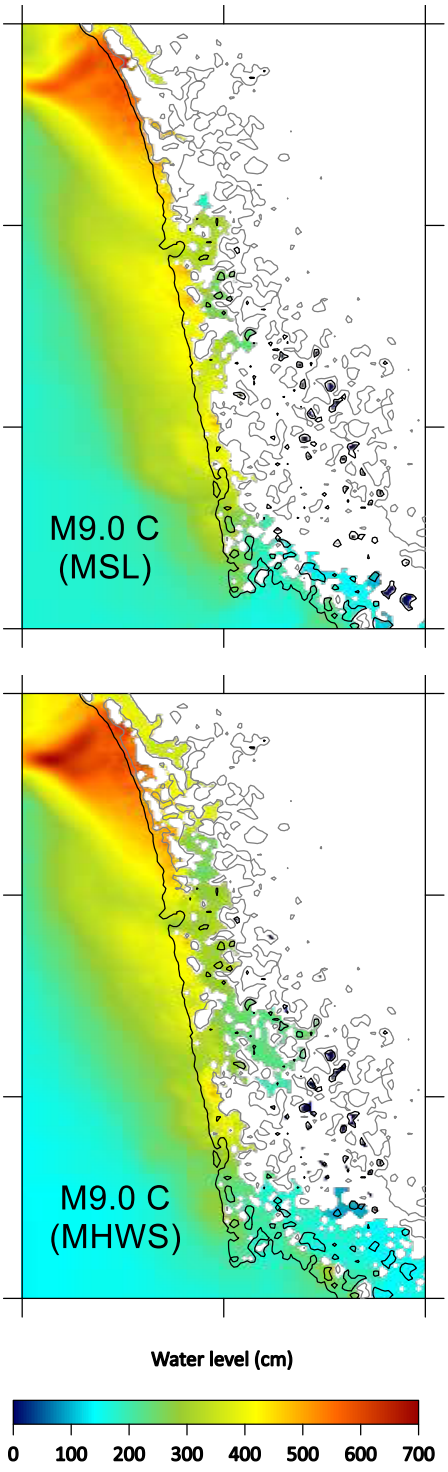

Figure 12. Comparison of maximum coastal inundation extents for the M9.0-C scenario under different tidal conditions: (a) simulation initialized at Mean Sea Level (MSL), highlighting the +3.5 m elevation contour; and (b) simulation initialized at Mean High Water Springs (MHWS), highlighting the +4.5 m elevation contour.

5. Conclusion

This study presented a high-resolution deterministic tsunami hazard assessment for the Kooh Mobarak area and its associated critical marine infrastructure, located strategically near the Strait of Hormuz. By utilizing the ComMIT/MOST numerical model within a nested grid framework and simulating twelve fault rupture scenarios across the Makran Subduction Zone (MSZ), the research provides a detailed quantification of the hydrodynamic risks and challenges conventional assumptions regarding the hazard distribution in the region. The principal conclusions drawn from this investigation are summarized below.

First and foremost, the study explicitly confirms the critical threat posed by the Western Makran segment, a region often termed the "seismic gap" and frequently de-emphasized in regional assessments. The simulation results demonstrate that the proximity of the source plays a more decisive role than magnitude alone for the Kooh Mobarak coastline. A rupture in the Western segment (M_w 8.9) generates wave heights (~2.79 m) and current velocities at ST3 location that are statistically comparable to those of a catastrophic Central Makran rupture (M_w 9.0). Given the minimal geometric attenuation and the directivity of the energy beam towards the north, the Western segment must be regarded as the governing near-field hazard source. Furthermore, the short arrival time of approximately 33 to 40 minutes leaves a negligible window for evacuation, highlighting the inadequacy of distant regional warning centers and the urgent necessity for a dedicated, local early warning system integrated with real-time cabled seafloor sensors.

Second, the analysis of nearshore hydrodynamics reveals that the hazard profile is dominated by non-linear shallow water transformations. The study identified a strong power-law correlation between wave height and current velocity in the nearshore zone, leading to extreme flow accelerations at the ST3 location (V_{max}>2.3 m/s). These velocities, driven by flow constriction and shoaling, are capable of exerting immense hydrodynamic drag forces on moored vessels and inducing rapid scouring at the toe of marine structures. Consequently, the structural design of armor units and mooring systems must prioritize resistance to these high-velocity sustained flows rather than relying solely on hydrostatic pressure distributions derived from wave height.

Third, the sensitivity analysis regarding initial tidal levels establishes a critical "Dual-Criterion" design philosophy for macrotidal regions. The results indicate that while the Mean High-Water Springs (MHWS) condition creates the worst-case scenario for coastal inundation, yielding a Total Water Level of approximately +5.32 m CD and extending the flood zone deep into the tidal creeks, it concurrently results in a slight attenuation (~15%) of the pure tsunami wave amplitude due to reduced shoaling effects. Conversely, the Mean Sea Level (MSL) condition, characterized by shallower depths, generates higher particle velocities and thus governs the design for scour protection and hydrodynamic drag. Therefore, a comprehensive resilience strategy for the Kooh Mobarak area must

utilize the MHWS scenario to determine crest elevations and flood defense heights, while employing the MSL scenario to verify the stability of subsea foundations and mooring loads.

In summary, this research underscores that the Kooh Mobarak region is exposed to a significant, multi-faceted tsunami hazard that cannot be adequately mitigated by generic regional guidelines. The findings advocate for a paradigm shift in the design codes for the Strait of Hormuz area, emphasizing the inclusion of the Western Makran scenarios and the compound effects of tidal interactions. Future research should complement this deterministic framework with a Probabilistic Tsunami Hazard Assessment (PTHA) to quantify the likelihood of these events over the facility's operational lifespan, thereby enabling a fully risk-informed decision-making process.

References

ASCE (American Society of Civil Engineers). (2017). Minimum Design Loads and Associated Criteria for Buildings and Other Structures (ASCE/SEI 7-16). Reston, VA: ASCE.

Byrne, D. E., Sykes, L. R., & Davis, D. M. (1992). Great thrust earthquakes and aseismic slip along the plate boundary of the Makran subduction zone. Journal of Geophysical Research: Solid Earth, 97(B1), 449-478.

El-Hussain, I., Omira, R., Deif, A., Al-Habsi, Z., Al-Rawas, G., Mohamad, A., ... & Baptista, M. A. (2016). Probabilistic tsunami hazard assessment along Oman coast from submarine earthquakes in the Makran subduction zone. Arabian Journal of Geosciences, 9(1), 1-14.

Frohling, E., & Szeliga, W. (2016). GPS constraints on interplate locking within the Makran subduction zone. Geophysical Journal International, 205(1), 67-76.

Heidarzadeh, M., Pirooz, M. D., Zaker, N. H., Yalciner, A. C., Mokhtari, M., & Esmaeily, A. (2008). Historical tsunami in the Makran Subduction Zone off the southern coasts of Iran and Pakistan and results of numerical modeling. Ocean Engineering, 35(8-9), 774-786.

Heidarzadeh, M., Pirooz, M. D., Zaker, N. H., & Yalciner, A. C. (2009). Preliminary estimation of the tsunami hazards associated with the Makran Subduction Zone at the northwestern Indian Ocean. Natural Hazards, 48(2), 229-243.

Kotani, M., Imamura, F., & Shuto, N. (1998). Tsunami run-up simulation and damage estimation by using GIS. Proceedings of Coastal Engineering, JSCE, 45, 356-360.

Kowalik, Z., & Proshutinsky, A. (2010). Tsunami-tide interactions: A case study of the 1964 Prince William Sound tsunami. Pure and Applied Geophysics, 167, 345-367.

Kukowski, N., Schillhorn, T., Huhn, K., von Rad, U., Husen, S., & Flueh, E. R. (2001). Morphotectonics and mechanics of the central Makran accretionary wedge off Pakistan. Marine Geology, 173(1-4), 1-19.

Mokhtari, M. (2011). Tsunami hazard in the Makran Subduction Zone. International Journal of Earth Sciences, 100(4), 865-874.

Okada, Y. (1985). Surface deformation due to shear and tensile faults in a half-space. Bulletin of the Seismological Society of America, 75(4), 1135-1154.

Okal, E. A., & Synolakis, C. E. (2008). A theoretical analysis of tsunamis from hypothetical landslides at the Makran Subduction Zone. Geophysical Journal International, 173(2), 654-672.

Penney, C., & Copley, A. (2019). Lateral variation in the mechanics of the Makran accretionary prism. Earth and Planetary Science Letters, 508, 60-71.

Rajendran, C. P., Ramanamurthy, M. V., Reddy, N. T., & Rajendran, K. (2008). Hazard implications of the late arrival of the 1945 Makran tsunami. Current Science, 95(12), 1739-1743.

Rashidi, A., Ortwin, R., & Sadeghi, M. (2020). Coastal vulnerability assessment of the Chabahar Bay due to tsunami hazard. Natural Hazards, 103, 2215–2234.

Smith, G. L., McNeill, L. C., Wang, K., He, J., & Henstock, T. J. (2013). Thermal structure and megathrust seismogenic potential of the Makran subduction zone. Geophysical Research Letters, 40(7), 1528-1533.

Titov, V. V., & Gonzalez, F. I. (1997). Implementation and testing of the Method of Splitting Tsunami (MOST) model. NOAA Technical Memorandum ERL PMEL-112.

Titov, V. V., & Synolakis, C. E. (1998). Numerical modeling of tidal wave runup. Journal of Waterway, Port, Coastal, and Ocean Engineering, 124(4), 157-171.

Titov, V. V., Moore, C. W., Greenslade, D. J. M., Pattiaratchi, C., Badal, R., Synolakis, C. E., & Kânoğlu, U. (2011). A new 2004 Indian Ocean tsunami forecast model. Geophysical Journal International, 187, 1051-1058.

Vernant, P., Nilforoushan, F., Hatzfeld, D., Abbassi, M. R., Vigny, C., Masson, F., ... & Bayer, R. (2004). Present-day crustal deformation and plate kinematics in the Middle East constrained by GPS measurements in Iran and northern Oman. Geophysical Journal International, 157(1), 381-398.

Wells, D. L., & Coppersmith, K. J. (1994). New empirical relationships among magnitude, rupture length, rupture width, rupture area, and surface displacement. Bulletin of the Seismological Society of America, 84(4), 974-1002.